COMPUTATIONAL SIMULATION OF SHAPED METAL DEPOSITION

Víctor D. Fachinotti and Alberto Cardona

Centro Internacional de Métodos Computacionales en Ingeniería (CIMEC-INTEC) – Universidad Nacional del Litoral (UNL) / Consejo Nacional de Investigaciones Científicas y Técnicas (CONICET) Güemes 3450, S3000GLN Santa Fe, Argentina – E-mails: vfachino@intec.unl.edu.ar, acardona@intec.unl.edu.ar, http://www.intec.unl.edu.ar

Keywords: SMD, welding, FEM.

Abstract. Shaped Metal Deposition (SMD) is a novel technology to build near-net shaped pieces by weld deposition. The pieces we are interested in are aerospace components made of Titanium alloys. Given such expensive material, the reduction of scraps thanks to near-net shaping is crucial. Although already operational, the process still requires a great deal of manual intervention and control. Our research focus then on developing computational models of the physical phenomena involved in SMD as a first step to its automatic control.

This work deals with the modelling of the thermal field developed during SMD, which is basically a multi-pass TIG-welding process. The problem to be solved is the transient heat conduction induced by a highly concentrated heat source representing the welding arc. Being a multi-pass welding problem, we have to deal with cyclic temperature variations, including successive melting and solidification.

The problem is solved using linear triangular finite elements, with the phase change terms evaluated using the discontinuous integration technique developed by the authors in a previous work.

1 INTRODUCTION

This paper describes the numerical procedure implemented to calculate the space and time temperatures distribution during the Shaped Metal Deposition (SMD) process.

We start describing the theoretical basis of the heat transfer problem during welding, and the way in which phase change is taken into account.

Afterwards, the parametrization of the bead geometry is described, both for the single layer and for the multilayer cases.

The heat source model is next given, and an example is developed for the single layer deposition case, with calibration with results from experiences.

Then, a multilayer case is treated, and finally the case of three-dimensional representation of the shape metal deposition process is analyzed.

2 SOLUTION OF THE HEAT TRANSFER PROBLEM IN SMD

We aim to determine the evolution of the temperature inside the deposited bead and the substrate, which constitute together the domain of analysis, say Ω. Let us note the domain Ω increases with each welding pass: at the beginning, Ω consists only of the substrate.

The temperature $T(x, y, z, t)$ at any point $(x, y, z) \in \Omega$ at the instant t is given by the solution of the transient heat conduction equation

$$\frac{\partial H}{\partial t} - \operatorname{div}\left(\boldsymbol{\kappa}\operatorname{grad} T\right) = q \qquad \forall (x, y, z) \in \Omega,\ t < 0 \tag{1}$$

where H is the enthalpy, k is the thermal conductivity tensor and q is the heat source, produced by the welding torch. The heat transfer problem is completed by specifying the initial temperature of the substrate (that constitutes the domain of analysis at the initial time instant $t = 0$):

$$T(x, y, z, 0) = T_0(x, y, z) \qquad \forall (x, y, z) \in \Omega \tag{2}$$

and the conditions imposed on the boundary Γ of Ω:

- the prescribed temperature at the portion Γ_T of Γ:

$$T(x, y, z, t) = \bar{T}(x, y, z, t) \qquad \forall (x, y, z) \in \Gamma_T,\ t > 0 \tag{3}$$

- convection and/or radiation through the portion Γ_{cr} of Γ:

$$- \boldsymbol{\kappa}\operatorname{grad} T \cdot \mathbf{n} = h(T - T_{cr}) \qquad \forall (x, y, z) \in \Gamma_{cr},\ t > 0 \tag{4}$$

  where $\mathbf{n}$ denotes the outer normal to Γ, h the convection/radiation coefficient (in general, dependent of temperature), and T_{cr} is either the temperature of the environment or that of the radiant body.

In order to make the heat conduction equation depend only on the temperature, we introduce the enthalpy function defined as follows

$$H(T) = \int_0^T \rho c_p(\tau)\, \mathrm{d}\tau + \rho L f_l(T) \tag{5}$$

where ρc_p is the heat capacity, L the latent heat of solidification and f_l the volume fraction of liquid, which is assumed to vary linearly with temperature between the solidus temperature T_{sol} and the liquidus temperature T_{liq}, i.e.:

$$f_l = \begin{cases} 0 & \text{for } T < T_{sol} \\ \frac{T - T_{sol}}{T_{liq} - T_{sol}} & \text{for } T_{sol} \leq T \leq T_{liq} \\ 1 & \text{for } T > T_{liq} \end{cases} \tag{6}$$

Enthalpy should also account for the latent heat involved in solid phase transformations, but this is negligible compared to the latent heat of fusion.

The computational solution of the heat conduction equation (1) requires its discretization, i.e., to convert it to an approximate algebraic form. Spatial discretization is achieved using the finite element method (FEM). Specifically, we use the linear triangular finite elements with discontinuous integration proposed by Fachinotti et al. (1999), which allows an improved representation of solidification problems. For time integration, the fully implicit backward-Euler scheme is used.

In the case of processes like welding, casting, etc., which involve melting and solidification, the heat transfer problem is highly non-linear due to the steep variation of the enthalpy in the solidification range. The temperature dependence of thermal properties like the thermal conductivity, the heat capacity and the heat convection/radiation coefficient also contributes to the non-linearity of the problem. In this work, we solve the discretized non-linear transient heat conduction equation in an iterative way using the Newton-Raphson method, which ensures a quadratic convergence rate to the desired solution.

3 *A-PRIORI* DEFINITION OF THE BEAD GEOMETRY

Before modelling any problem, we need to define the domain of analysis. In our case, it consists of the substrate and the bead. While the dimensions of the substrate are known prior to deposition, the bead is created along the process and its geometry depends on the combined effects of arc pressure, droplet impact, weld pool gravity, and surface tension. Predicting the bead geometry on the base of these effects is out of the scope of the present work. Therefore, by making some empirical assumptions, we will define the bead geometry as accurate as possible using the available information.

First, neglecting the density variations between the solid and liquid phases of the filler material, the cross section area A_i of the bead i can be determined in terms of known variables like the welding velocity V_w, the diameter ϕ_f of the wire, and the wire feed rate V_f using the formula:

$$A_i = \frac{\pi}{4} \phi_f^2 \frac{V_f}{V_w} \tag{7}$$

Once A_i is known, Wu et al. (2007) proposed to assimilate the cross section of a single-pass bead to a parabolic sector. Under this assumption, it remains only one unknown, either the width w_i or the height h_i of the bead, or equivalently the flatness ratio $\alpha_i = w_i/h_i$.

Unfortunately, the single-pass bead geometry can be more complicated than a parabolic sector, as shown in Figure 1 where splines were used to fit accurately the surface of the bead, leaving multiple unknowns.

Further complexity arises when dealing with multi-pass welds, like the one shown in Figure 2.
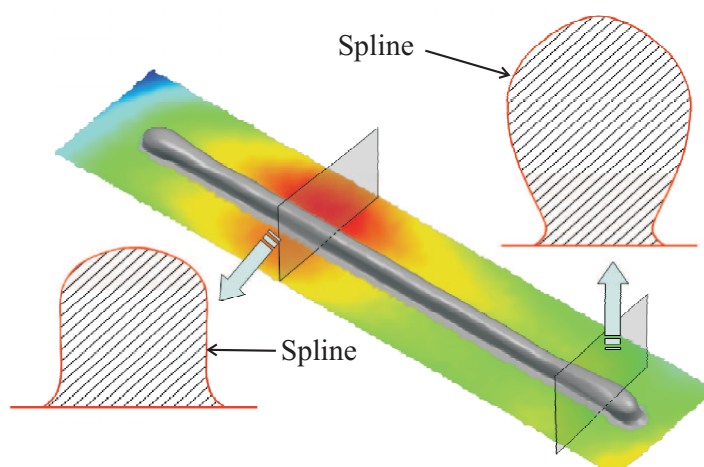
Figure 1: Single bead whose cross sectional geometry can not be represented by a parabolic sector (Tham, 2008).

Figure 2: Etched cross section of specimen 05 obtained by SMD.

In either case, an accurate *a-priori* estimate of geometric unknowns can be made by applying neural networks or regression analysis from experimental measurements (Gunaraj and Murugan, 2000; Lee and Um, 2000; Kim et al., 1995). To this end, a large-enough database must be built, containing the values of the parameters needed to define the bead geometry in terms of the control variables of the process (welding velocity, wire feed rate, wire diameter, wire material, amperage, voltage, etc.). This task is currently in progress in the project. Meanwhile, we make some further assumptions to be able to go on with computations.

Let us consider for instance the bead 05 depicted in Figure 2, obtained by SMD with 35 deposition layers. First, we will assume the width w of the bead to be known. Then, we define the generic layer i as the sector lying between the curves $y_{i-1}(x)$ and $y_i(x)$, as shown in Figure

3. We assume both curves defined by the parabolic laws:

$$y_{i-1}(x) = y_{i-1}^{max} - 4\frac{\Delta y_{i-1}}{w^2}x^2 \tag{8}$$

$$y_i(x) = y_i^{max} - 4\frac{\Delta y_i}{w^2}x^2 \tag{9}$$

with $y_0(x) \equiv 0$ as the lower boundary of the first layer, and $-w/2 \le x \le w/2$.
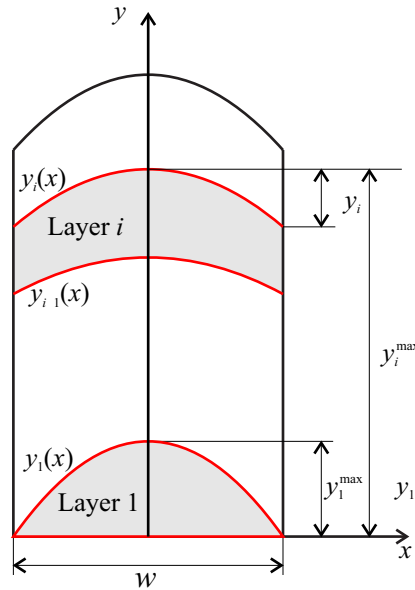
Figure 3: Schema of the first and the i-th deposition layers.

The area of the i-th layer is

$$A_i = w\left(y_i^{max} - \frac{\Delta y_i}{3}\right) - \sum_{j=1}^{i-1} A_j \tag{10}$$

Above formula also accounts for the first layer, which can be assimilated to a parabolic single-pass bead with $y_i^{max} = \Delta y_i = 0$ and $A_0 = 0$.

By equating equations (7) and (10), and by introducing the flatness ratio $\alpha_i = w/\Delta y_i$, we obtain the equation

$$w\left(y_i^{max} - \frac{w}{3\alpha_i}\right) - \sum_{j=1}^{i-1} A_j = \frac{\pi}{4}\phi_f^2\frac{V_f}{V_w} \tag{11}$$

with α_i and y_i^{max} as unknowns. Then, as done by Wu et al. (2007) with a single-pass bead, we can adopt *a priori* a value for the flatness ratio α_i on the base of experimental observations. From Figure 1 it is possible to estimate the final flatness ratio $\alpha_N \approx 2.81$, with the subscript N referring to the total number of deposition layers. On the other hand, the flatness of the first layer, assumed to be a parabolic sector, is given by

$$\alpha_1 = \frac{2}{3}\frac{w^2}{A_1} = \frac{8}{3}\frac{w^2}{\pi\phi_f^2} \tag{12}$$

We assume now a law for the variation of the flatness ratio α_i from the first to the last layer. Until having enough data to define this law on the base of observations, we will assume the flatness of the i-th layer defined by the linear law

$$\alpha_i = \alpha_1 + \frac{\alpha_N - \alpha_1}{N-1}(i-1) \tag{13}$$

From equation (11), we obtain

$$y_i^{max} = \frac{1}{w}\left(\frac{\pi}{4}\phi_f^2\frac{V_f}{V_w} + \sum_{j=1}^{i-1}A_j\right) + \frac{w}{3\alpha_i} \tag{14}$$

Knowing $\phi_f = 12$ mm, $V_w = 0.3$ m/min, and $V_f = 2.513$ m/min, these assumptions produce the multi-layered geometry depicted in Figure 4. The computed total height is about 33.1 mm, i.e., 6.4% greater than the measured one, which is considered as a satisfactory fitting considering the limited available information.
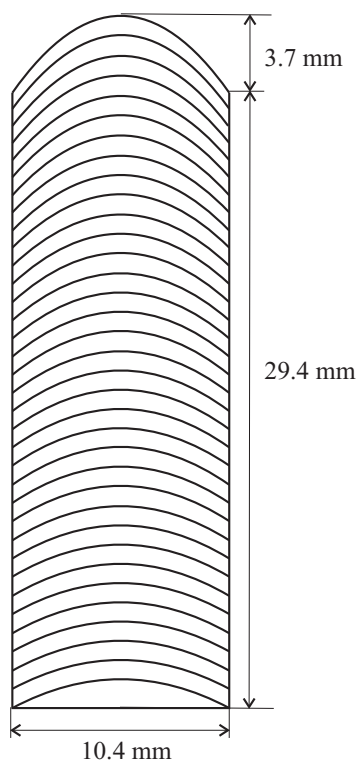
Figure 4: *A-priori* estimation of the multi-layered geometry of bead 05.

4 ARC-WELDING HEAT SOURCE MODEL

In this work, we use one of the most cited heat source models for welding, proposed by Goldak et al. (1984), which is defined as

$$q(\tilde{x}, \tilde{y}, \tilde{z}, t) = \frac{6\sqrt{3}Q}{\pi\sqrt{\pi}ab} \times \begin{cases} \frac{f_f}{c_f}\exp\left[-3\frac{\tilde{x}^2}{a^2} - 3\frac{\tilde{y}^2}{b^2} - 3\frac{(\tilde{z})^2}{c_f^2}\right], & \text{for } \tilde{z} > 0, \\ \frac{f_r}{c_r}\exp\left[-3\frac{\tilde{x}^2}{a^2} - 3\frac{\tilde{y}^2}{b^2} - 3\frac{(\tilde{z})^2}{c_r^2}\right], & \text{for } \tilde{z} < 0. \end{cases} \tag{15}$$

where $\tilde{O}$-$\tilde{x}\tilde{y}\tilde{z}$ is a moving orthogonal system of coordinates with origin $\tilde{O}$ coincident with the trace of the torch onto the surface of the weld, Q is the total heat input rate, f_f (resp. $f_r = 2 - f_f$) is the fraction of the heat deposited in the front (resp. rear) quadrant, and a, b, and c_f (resp. c_r) are the radii of the ellipsoid in the front (resp. rear) quadrant (see Figure 5 for details). This law describes a Gaussian distribution of heat power density inside a double-ellipsoidal volume.

Let us note that equation (15) was developed assuming the weld piece to be the semi-infinite body $y \geq 0$ such that

$$\int_{-\infty}^{\infty} \int_{0}^{\infty} \int_{-\infty}^{\infty} q(x, y, z) \, \mathrm{d}x \, \mathrm{d}y \, \mathrm{d}z = Q \tag{16}$$

If the volume Ω where Q is spread consists not only of the substrate but also of the deposited bead, Ω can not longer be assimilated to a semi-infinite body, and then

$$\chi = \frac{1}{Q} \int_{\Omega} q(x, y, z) \, \mathrm{d}\Omega \neq 1 \tag{17}$$

In this case, equation (15) must be corrected by dividing the r.h.s. by χ in order to ensure that the total heat input rate remains effectively Q.
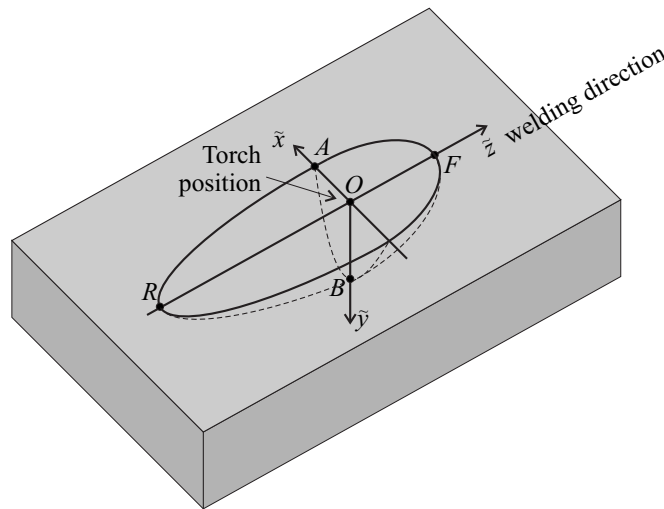
Figure 5: Double-ellipsoidal heat source (Goldak et al., 1984).

The rate of heat induced by an arc welding source can be computed as

$$Q = \eta V I \tag{18}$$

where η is the efficiency, V is the voltage and I the intensity of current.

4.1 Calibration of the heat source

Another important step prior to simulate a particular welding process like SMD for instance, is the calibration of the heat source. The calibration of the double-ellipsoidal heat source model implies to determine the value of the unknown parameters in equation (15) which are ordered in the vector

$$\mathbf{c} = [\eta \ V \ a \ b \ c_f \ c_r \ f_f] \tag{19}$$

For each choice of $\mathbf{c}$, we can compute numerically the temperature field and derive from it the liquidus isotherm enclosing the fusion zone (FZ). These results are ordered in the vector

$$\mathbf{g}(\mathbf{c}) = [w_{FZ} \; d_{FZ} \; T(x_1, y_1, z_1, t_1) \; \ldots \; T(x_i, y_i, z_i, t_j) \; \ldots] \tag{20}$$

where w_{FZ} and d_{FZ} are respectively the width and the depth of the FZ, and $T(x_i, y_i, z_i, t_j)$ is the temperature at the point (x_i, y_i, z_i) at the time instant t_j.

All these data are susceptible to be determined experimentally. Assuming that we know the experimental counterpart of the vector $\mathbf{g}$, say $\mathbf{g}_{exp}$, we must find the set of parameters $\mathbf{c}$ that minimizes the difference $\mathbf{g}_{exp} - \mathbf{g}(\mathbf{c})$ with respect to a certain norm. This yields a nonlinear optimization problem that can be solved using an appropriate optimization solver.

4.1.1　Example

Let us consider the single bead whose micrograph is shown in Figure 6, where we observe that $w_{FZ} = 9.62$ mm and $d_{FZ} = 1.75$ mm. There is not information about the temperature evolution along the process of deposition of this bead. Then, we will aim to make numerical results fit the measured width and depth of the FZ only.
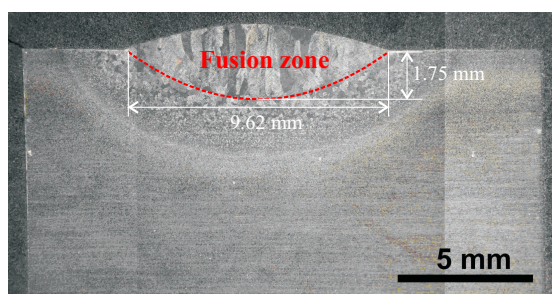
Figure 6: Etched cross sections of a single-pass bead evidencing the extension of the fusion zone.

Further, all the data is restricted to one section of the weld normal to the bead. Such reduced information has obliged us to introduce additional assumptions concerning the distribution of heat ahead and behind the welding arc. First, we will assume $c_r = 4c_f$, as suggested by Goldak et al. (1984). Then, by requiring the continuity of the function q given by equation (15) at $\tilde{z} = 0$ (interface between the front and rear quadrants) as suggested by Nguyen et al. (1999), we have

$$f_f = 2\frac{c_f}{c_f + c_r} = 0.4 \tag{21}$$

Further reduction of the number of variables is achieved by grouping efficiency and voltage in one single variable $V_{red} = \eta V$. Then, the vector of parameters to be calibrated takes the form

$$\mathbf{c} = [V_{red} \; a \; b \; c_f] \tag{22}$$

and the calibration problem can be stated as: find $\mathbf{c}_{cal}$ such that

$$\left\| \begin{array}{c} w_{FZ}(\mathbf{c}_{cal}) - w_{FZ}^{exp} \\ d_{FZ}(\mathbf{c}_{cal}) - d_{FZ}^{exp} \end{array} \right\| = \min_c \left\| \begin{array}{c} w_{FZ}(\mathbf{c}) - w_{FZ}^{exp} \\ d_{FZ}(\mathbf{c}) - d_{FZ}^{exp} \end{array} \right\| \tag{23}$$

where $\|\mathbf{v}\|$ denotes the L_2-norm of the vector $\mathbf{v}$. The values $w_{FZ}(\mathbf{c})$ and $d_{FZ}(\mathbf{c})$ are computed for each choice of $\mathbf{c}$ on the base of the temperature field obtained as output of the heat transfer
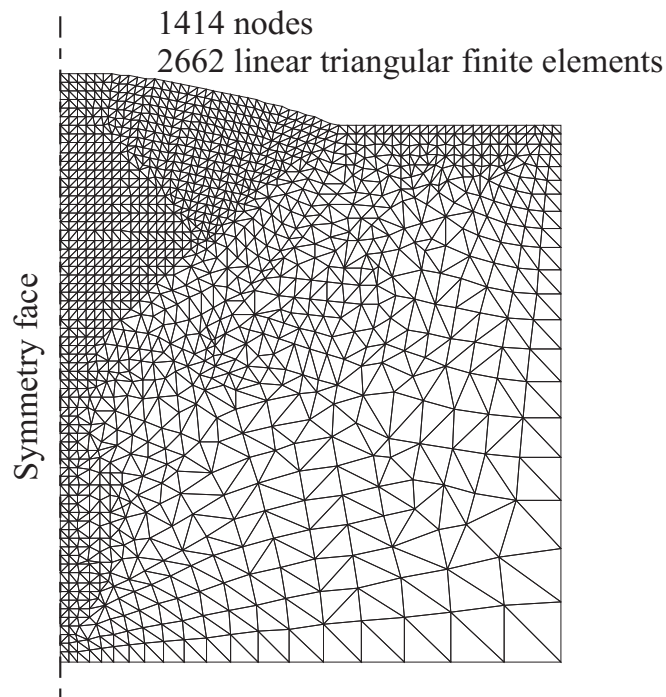
Figure 7: Finite element mesh used in the analysis.

finite element analysis. We use the mesh of linear triangular finite elements depicted in Figure 7.

Solving problem (23), we obtain $w_{FZ}(\mathbf{c}_{cal}) = 8.65$ mm, and $d_{FZ}(\mathbf{c}_{cal}) = 1.59$ mm (i.e., a maximum relative error of 10.04%), for the following set of calibrated values: $V_{red} = 7.99$ V, $a = 10.34$ mm, $b = 1.85$ mm, $c_f = 0.64$ mm. Figure 8 shows the estimated extension of the FZ as well as the heat power density distribution. Let us remark that the extension of the double ellipsoid predicted here is not comparable to the extension of the FZ, contradicting Goldak et al. (1984). Anyway, more experimental data, especially temperature measurements in different cross sections, will be needed to assert this conclusion.
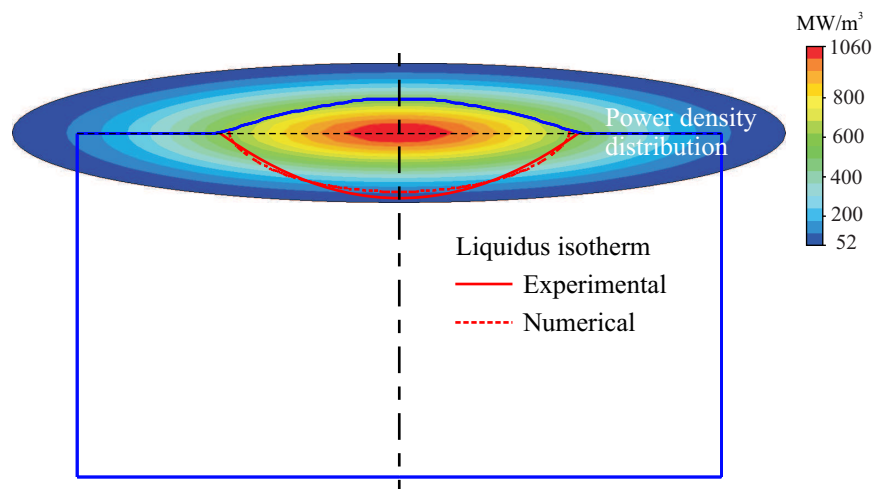
Figure 8: Calibration results

5   APPLICATION

Having defined the geometry of the bead and calibrated the heat source model, we can accomplish the heat transfer analysis. Let us consider the square hollow cylinder made of Ti-6Al-V alloy, schematized in Figure 9. Each cylinder wall is approximately 140 mm long, 10.4 mm wide and 31 mm tall. There were needed 35 deposition passes to obtain this piece, following the path shown on the right of Figure 9.
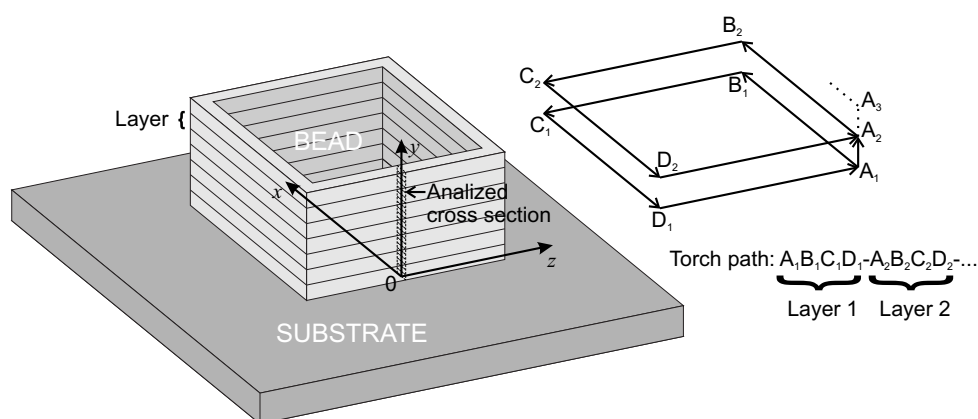
Figure 9: Schema of a hollow square cylinder produced by SMD. On the right, path of the welding torch.

The aim of this work is to determine the thermal field at a cross section located in the middle of the wall. The micrograph of the top 22.5 mm of this section is that shown in Figure 2. Since such section is located far enough from the corners, it can be approximated as belonging to an indefinitely long straight bead, neglecting 3D effects. The so-obtained 2D model takes further advantage of the almost symmetric geometry of the cross section with respect to is center plane. The resulting numerical model is shown in Figure 10.
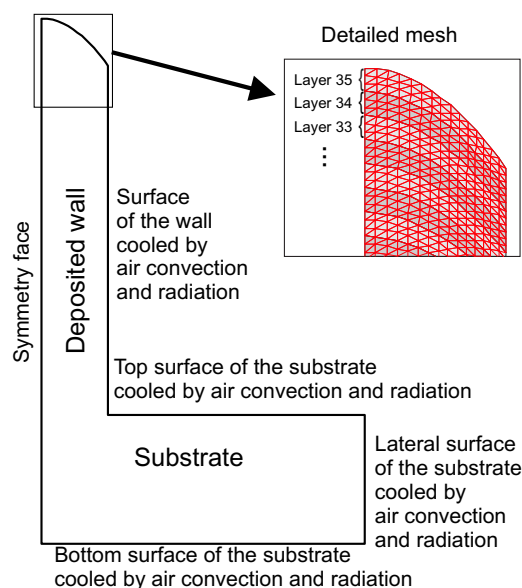
Figure 10: 2D model of the deposited wall and the substrate. The dashed region of the wall corresponds to half of the section.

Thermal properties of Ti-6Al-4V as a function of temperature were obtained from Material Property Database (MPDB) (Jahm Software Inc., 2009).

Following Goldak et al. (1984, 1986); Bonifaz (2000); Fan and Kovacevic (2004); Wu and Yan (2004); Wu et al. (2004), combined convection and radiation are prescribed as boundary conditions, defining a convection-radiation heat transfer coefficient

$$h_{cr} = 2.41 \times 10^{-4} \epsilon T^{1.61} \tag{24}$$

where T must be entered in K, and $\epsilon = 0.9$ is the surface emissivity.

The welding velocity is 0.3 m/min, so that each deposition layer is completed after 112 sec. Once a layer is completed, the mesh is increased by the subsequent layer. The 35th (last) layer is completed at 3920 sec. Then, the torch is moved away, and the weld begins to cool in the SMD chamber atmosphere.

Analysis is extended 2240 sec during this period. A time step of 0.5 sec is adopted, so that 12320 time steps are needed to cover the whole time interval of interest (this fact was relevant to choose a 2D model).

Figure 11 shows the thermal state of the bead from the first moment the temperature falls down the liquidus temperature until the moment when no more phase transformations are expected.

6 CONCLUSIONS

This work gives a first insight of the complex thermal phenomena that take place in the Shaped Metal Deposition (SMD) process. The three step to treat the problem were considered: *a-priori* definition of the geometry, calibration of the heat source and simulation.

Concerning the geometry, emphasis was put on defining the geometry of the multi-layered bead as accurate as possible with the available data. In the future, we expect to survey enough data to estimate more complex geometries that appear when the control parameters (welding speed and direction, wire feed rate, wire diameter, heat input, etc.) vary along the process.

An algorithm for calibration of the heat source model was also developed. Once calibrated, the numerical model was able to fit the geometry of the FZ with enough accuracy. The geometry of the double-ellipsoid was found to be not close to that of the FZ, contrary to other authors's observations. However, more experimental information is needed to confirm current results.

Finally, the numerical simulation of the problem was performed using a 2D cross-section finite element model. The use of a 2D model allows to consider the whole time interval of interest (about 2 hours) using a quite fine time step (0.5 sec) for accuracy reasons.

ACKNOWLEDGEMENTS

REFERENCES

Bonifaz E.A. Finite element analysis of heat flow in single-pass arc welds. *Welding Research Supplement*, pages 121–125, 2000.

Fachinotti V.D., Cardona A., and Huespe A.E. A fast convergent and accurate temperature model for phase-change heat conduction. *Int. J. Numer. Methods Engrg.*, 44:1863–1884, 1999.

Fan H.G. and Kovacevic R. A unified model of transport phenomena in gas metal arc welding including electrode, arc plasma and molten pool. *J. Phys. D: Appl. Phys.*, 37:2531–2544, 2004.

Goldak J., Bibby M., Moore J., House R., and Patel B. Computer modelling of heat flow in welds. *Metallurgical Transactions B*, 17:587–600, 1986.

Goldak J., Chakravarti A., and Bibby M. A new finite element model for welding heat sources. *Metallurgical Transactions B*, 15:299–305, 1984.

Gunaraj V. and Murugan N. Prediction and optimization of weld bead volume for the submerged arc process – part 1. *Welding Research Supplement*, pages 286–294, 2000.

Jahm Software Inc. Mpdb v6.69. 2009.

Kim I.S., Son J.S., Park C.E., Kim I.J., and Kim H.H. An investigation into an intelligent system for predicting bead geometry in GMA welding process. *Journal of Materials Processing Technology*, 159:113–118, 1995.

Lee J. and Um K. A comparison in a back-bead prediction of gas metal arc welding using multiple regression analysis and artificial neural network. *Optics and Lasers in Engineering*, 34:149–158, 2000.

Nguyen N.T., Ohta A., Matsuoka K., Suzuki N., and Maeda Y. Analytical solutions for transient temperature of semi-infinite body subjected to 3-D moving heat sources. *Welding Research Supplement*, pages 265–274, 1999.

Tham W.S. Private communication. *The Advanced Manufacturing Research Centre (AMRC) with Boeing, University of Sheffield, UK*, pages 223–231, 2008.

Wu C.S., Chen J., and Zhang Y.M. Numerical analysis of both front- and back-side deformation of fully-penetrated GTAW weld pool surfaces. *Computational Materials Science*, 39(3):635–642, 2007.

Wu C.S. and Yan F. Numerical simulation of transient development and diminution of weld pool in gas tungsten arc welding. *Modelling Simul. Mater. Sci. Eng.*, 12:13–20, 2004.

Wu C.S., Zhao P.C., and Zhang Y.M. Numerical simulation of transient 3-D surface deformation of a completely penetrated GTA weld. *Welding Research*, pages 330–335, 2004.
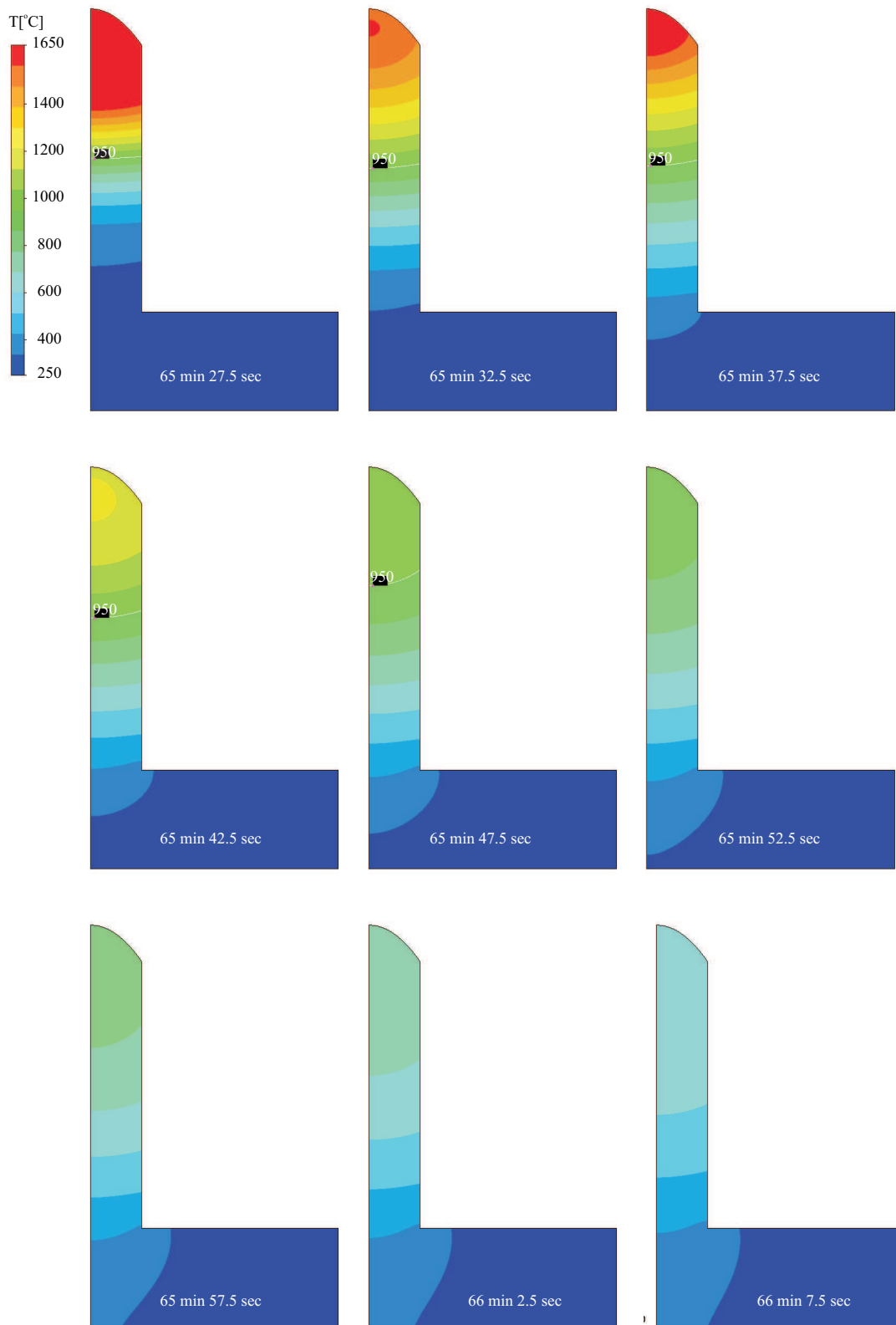
Figure 11: Temperature field and location of the isotherm of 950ºC (β-transus) immediately after the complete solidification of the bead.